PCCP

ROYAL SOCIETY OF CHEMISTRY

PAPER

View Article Online
View Journal

Check for updates

Cite this: DOI: 10.1039/d6cp01436d

Uptake of ammonia by mixed sulfate–bisulfate cluster cations under multicollisional conditions: approaching equilibrium particle formation in ion traps

Kevin Li, [a] Gabriel Schöpfer, [b] Milan Ončák [b] and Jozef Lengyel *[a]

Ammonia is a key base driving atmospheric new particle formation by stabilizing sulfur-containing clusters through acid–base interactions. Here we investigate ammonia uptake by mass-selected sodium sulfate–bisulfate cluster cations using an ion trap operated under multicollisional conditions at room temperature, complemented by quantum chemical calculations. Mixed sulfate–bisulfate clusters serve as a model system that allows systematic control of the number of acidic protons, providing insight into the mechanistic aspects of ammonia uptake. The results show that the maximum ammonia uptake strongly correlates with the number of bisulfate units in the cluster, demonstrating that acidic protons govern ammonia stabilization through ammonium–(bi)sulfate ion pair formation. Thermochemical calculations confirm that the ammonium formation is energetically highly favorable. Kinetic measurements demonstrate sequential ammonia uptake, in which the first adsorption step is rate-limiting and concurrently stabilizes the cluster, leading often to lower evaporation rates in subsequent steps. Increasing the bisulfate content enables additional uptake steps but reduces the overall reaction rate. The Gibbs free energies of ammonia uptake derived from experiment are in very good agreement with the calculated values, suggesting that the system is approaching equilibrium under the experimental conditions.

Received 17th April 2026,
Accepted 3rd June 2026

DOI: 10.1039/d6cp01436d

rsc.li/pccp

Open Access Article. Published on 04 June 2026. Downloaded on 6/26/2026 5:20:09 PM.
This article is licensed under a Creative Commons Attribution 3.0 Unported Licence.

1 Introduction

Atmospheric aerosol particles are central to climate and air quality due to their influence on radiative forcing, cloud formation, and heterogeneous chemistry.[1,2] A substantial fraction of atmospheric aerosols is produced *via* new particle formation, which is initiated by the clustering of low-volatility vapors and subsequently driven by molecular-scale interactions that stabilize nascent clusters against evaporation.[3,4] Sulfuric acid and ammonia act as key contributors to early stage cluster growth, as strong acid–base interactions efficiently stabilize molecular clusters and promote particle formation.[3]

While the binary nucleation of sulfuric acid and ammonia has been studied extensively,[5–9] far less is known about its role in mixed multicomponent clusters, particularly in systems where synergistic effects may become important.[10] These are commonly observed when the combined presence of multiple chemical components leads to properties that cannot be predicted from the individual constituents alone. Nitric acid and ammonia can form ammonium nitrate clusters, but HNO_3–NH_3 nucleation alone is too slow to compete with H_2SO_4–NH_3 nucleation.[11] When all three vapors are present, synergistic interactions lead to nucleation rates that are orders of magnitude higher than those of any binary system.[12] Synergistic effects are also observed in H_2SO_4 nucleation involving different bases. Amines typically stabilize sulfuric acid clusters more effectively than ammonia due to their higher basicity.[13–15] However, laboratory studies have shown that nucleation is further enhanced when ammonia and amines are present simultaneously, compared to systems containing either base alone.[8,16] These observations indicate that nucleation efficiency is not governed solely by base strength or concentration, but also arises from cooperative interactions among cluster constituents. Such effects may involve certain molecules acting as hydrogen-bonding bridges.[17] For example, ammonia can form more hydrogen bonds than sterically hindered amines, which may facilitate the formation of more strongly bound cluster networks.[18]

To examine the nature of such synergistic effects, we study ammonia uptake by mass-selected sodium sulfate–bisulfate cluster cations using an ion trap mass spectrometer. Although field measurements do not indicate that sodium sulfate is involved in atmospheric new particle formation, it provides a relevant proxy for sulfate seed aerosols, as it forms during the

[a] School of Natural Sciences, Technische Universität München, Lichtenbergstr. 4, 85748 Garching, Germany. E-mail: jozef.lengyel@tum.de
[b] Institut für Ionenphysik und Angewandte Physik, Universität Innsbruck, Technikerstr. 25/3, 6020 Innsbruck, Austria

Open Access Article. Published on 04 June 2026. Downloaded on 6/26/2026 5:20:09 PM.
This article is licensed under a Creative Commons Attribution 3.0 Unported Licence.

atmospheric aging of sea-spray particles following reaction of sodium chloride with sulfuric acid.[19–22] These particles often exhibit a broad range of acidities resulting from partial conversion of sulfate to bisulfate,[23] which promotes heterogeneous chemistry such as the formation of organosulfates during the reactive uptake of oxidized organic molecules on acidic sodium sulfate.[24]

Our focus is on mixed clusters containing two distinct inorganic constituents to investigate how their coexistence influences ammonia uptake, cluster stabilization, and nucleation rates. Mass selection enables direct insight into how sulfate and bisulfate content governs ammonia uptake and uncovers effects that are otherwise masked in studies of broad cluster distributions. It has been shown that ion trap experiments under ultrahigh vacuum conditions are well suited for probing size-dependent kinetics of cluster growth in subnanometer particles.[25–28] In the present work, ammonia uptake is investigated under multicollisional conditions to account for the influence of frequent gas-cluster collisions on cluster stabilization, temperature control, and evaporation pathways relevant to the atmospheric new particle formation.

2 Experimental and computational details

The experiments were performed on an ion trap mass spectrometer equipped with an electrospray ionization (ESI) source.[29] The analyte solution was introduced through a fused silica capillary at a flow rate of 1.5 μL min^{-1} with a spray voltage of 2.4 kV. Mixed sodium sulfate–bisulfate cluster ions were generated in positive ion mode from a 1 mM sodium sulfate solution prepared in water : MeOH (1 : 1, v/v) containing 0.005% (1 mM) sulfuric acid. Cluster ions generated at ambient pressure were transferred into the vacuum stage of the source chamber through a heated transfer capillary operated at 120 °C and a tube voltage of 150 V. In the first pumping stage, the ions were focused into a narrow beam using an S-lens stacked ring ion guide.[30] The skimmed cluster beam was guided by a set of rod-based ion guides into an electrostatic bender and directed into a quadrupole mass filter for mass selection.

The mass-selected ions were subsequently guided into a ring-electrode ion trap, where they were stored and thermalized through collisions with a helium buffer gas. Ammonia, mixed into the helium at concentrations between 0.01 and 10% v/v was continuously introduced into the trap at a total pressure of 2.1 Pa using a mass-flow controller. The absolute pressure inside the trap was monitored with a capacitance gauge, and under these conditions the ions rapidly equilibrated with the buffer gas. After defined storage times, reactant and product ions were analyzed using a reflectron time-of-flight mass spectrometer. To ensure consistent detection efficiencies, the delay between the ion trap extraction and the time-of-flight mass spectrometer was optimized for signal intensity. Multiple individual measurements, typically 400 scans, were averaged to obtain the final mass spectrum.

Reaction kinetics were measured by tracking ion abundances as a function of reaction time under pseudo-first-order conditions, with the neutral precursor in large excess. Relative abundances of reactant and product ions were obtained from time-resolved mass spectra. For single-step reactions, pseudo-first-order rate coefficients were determined from exponential fits to the decay of the reactant ion. More complex mechanisms, including consecutive and reversible reactions, were modeled using coupled differential rate equations describing the formation and depletion of all participating species. The equations are solved numerically by fitting to the experimental data, with the initial ion abundances treated as fit parameters. Multiple reaction models were evaluated to determine which mechanism best reproduces the experimental observations.

Interpretation of the experimental findings is supported by quantum chemical calculations. We considered clusters of $Na^+[Na_2SO_4]_m[NaHSO_4]_n$, m = 1–3, n = 1–4, each cluster with up to $n$$NH_3$ molecules. For n = 1, we also considered the adsorption of two NH_3 molecules. The structures were first generated using our in-house genetic algorithm (GA) program,[31] combined with the Extended Tight-Binding (xTB) program package[32] employing GFN2-xTB.[33] For the GA search, we used a population size of 50 clusters, 50 cycles, 50 recombinations and a mutation probability of 36% where original and mutated structure are kept in the population. From each GA run, structures within the relative energy of 0.7 eV (16.1 kcal mol^{-1}) were selected for recalculation at the r^{2}SCAN-3c level as implemented in ORCA.[34,35] The most stable 100 structures were always recalculated, every sixth structure was considered for higher-lying ones. If the most stable structure at the r^{2}SCAN-3c level was positioned in 20% of energetically highest-lying recalculated xTB structures, structures up to relative xTB energies of 1 eV (23.1 kcal mol^{-1}) were considered. Additionally, the most stable structures for a given m, n were considered to manually build clusters with a different number of adsorbed NH_3 molecules to consistently employ the most stable cluster patterns in a series with the same m and n. The mean absolute error of standard Gibbs energies of NH_3 adsorption for six different DFT approaches with respect to r^{2}SCAN-3c values lies within 2.6 kcal mol^{-1}, see Table S3.

To compare experimental and computational results directly, the standard Gibbs free energy change of NH_3 addition, ΔG°, was employed for the adsorption reaction:

$$M^+ + NH_3 \rightarrow [M + NH_3]^+ \quad (1)$$

The standard Gibbs free energy is related to the equilibrium constant K as follows, with all compounds being in the gas phase, with p_{NH_3} denoting the partial pressure of ammonia and p° the standard pressure:

$$\exp(-\Delta G^\circ/RT) = K = \frac{p^\circ p_{[M+NH_3]^+}}{p_{NH_3} p_{M^+}} \quad (2)$$

For the adsorption of $i$$NH_3$ molecules, an analogous expression arises:

$$\exp(-\Delta G^\circ/RT) = K = \frac{(p^\circ)^i p_{[M+iNH_3]^+}}{(p_{NH_3})^i p_{M^+}} \quad (3)$$

From the experimental data, ΔG° is derived from the observed ratio of peak intensities $\frac{I_{[M+NH_3]^+}}{I_{M^+}} \approx \frac{p_{[M+NH_3]^+}}{p_{M^+}}$ and

This journal is © the Owner Societies 2026

Open Access Article. Published on 04 June 2026. Downloaded on 6/26/2026 5:20:09 PM.
This article is licensed under a Creative Commons Attribution 3.0 Unported Licence.

the employed ammonia pressure. In the calculations, ΔG° is evaluated at 298.15 K using standard thermochemical approximations as implemented in ORCA.

It should be noted that both experimental and calculated Gibbs free energies are associated with considerable uncertainties. In the experiment, the uncertainty can be estimated from evaluating ΔG° at different relative NH_3 pressures, as K should be pressure-independent. In the calculations, apart from the influence of the quantum chemical method, the limited precision of harmonic approximation in predicting low-frequency vibrations represents a significant source of error in the entropic contribution. Furthermore, only the most stable minimum was considered, neglecting possible entropic effects arising from the presence of multiple isomers.

3 Results and discussion

3.1 Uptake capacity

Fig. 1 shows a mass spectrum of mixed sodium sulfate–bisulfate cluster ions. The signals correspond to (i) singly charged sodium sulfate clusters, $Na^+[Na_2SO_4]_m$, (ii) mixed sulfate–bisulfate clusters, $Na^+[Na_2SO_4]_m[NaHSO_4]_n$, and (iii) doubly charged mixed clusters, $Na_2^{2+}[Na_2SO_4]_m[NaHSO_4]_n$. In the mass spectrum singly charged $Na^+[Na_2SO_4]_m$ clusters containing up to approximately six sulfate units are observed. For mixed sulfate–bisulfate clusters, clearly distinguishable $Na^+[Na_2SO_4]_m[NaHSO_4]_n$ species are measured, with up to nine sulfate units and six bisulfate units. Doubly charged clusters become observable at sizes exceeding about five sulfate units, but with substantially lower intensities than that of the singly charged species. Only anhydrous cluster ions were detected, likely as a result of dehydration in the cluster source and ion trap.

For sulfate–bisulfate clusters, the size distribution of each cluster series exhibits a distinct maximum. For clusters containing a single sulfate unit, the ion intensity increases with increasing bisulfate number n, reaches a maximum at n = 6, and then decreases. Clusters with two, three, and four sulfate units show their highest intensities at n = 3, while clusters containing five sulfate units peak at n = 2. These trends are, however, influenced by the transmission characteristics of the mass spectrometer, given that ion transmission efficiency in the ion guides exhibits a pronounced m/z dependence under the applied instrumental settings.

In the next step, to probe the maximum ammonia uptake capacity, mass-selected mixed $Na^+[Na_2SO_4]_m[NaHSO_4]_n$ cluster ions were trapped and exposed to ammonia under conditions chosen to promote complete reaction (10% NH_3 in He, 400 ms to 3 s trapping time). Fig. 2 shows the number of NH_3 molecules taken up by mass-selected $Na^+[Na_2SO_4]_m[NaHSO_4]_n$ cluster ions. Clusters containing a single bisulfate unit typically bind one NH_3 molecule; however, for m = 2–3, a minor contribution corresponding to the uptake of a second NH_3 molecule is observed. Clusters containing two bisulfate units exhibit uptake capacities of two NH_3 molecules, independent of the number of sulfate units. For n = 3, stabilization of three NH_3 molecules occurs only for clusters with m = 2 and 3. In contrast, clusters with m = 1 and 4 bind only two NH_3 molecules. At higher bisulfate numbers (*e.g.*, n = 4), the maximum uptake capacity is observed for m = 2, with clusters binding up to four NH_3 molecules, whereas those with m = 3 bind three, and clusters with m = 1 accommodate only two NH_3 molecules. This behavior may reflect a lower adsorption energy, steric effects or specific orientations of the bisulfate units in the cluster that prevent ammonia from accessing additional binding sites. For n = 5, the maximum ammonia uptake reaches five NH_3 molecules, which is also observed for $Na^+[Na_2SO_4][NaHSO_4]_6$ cluster ions.

For a given number of bisulfate units n, variations in sulfate content do not lead to significant changes in the maximum

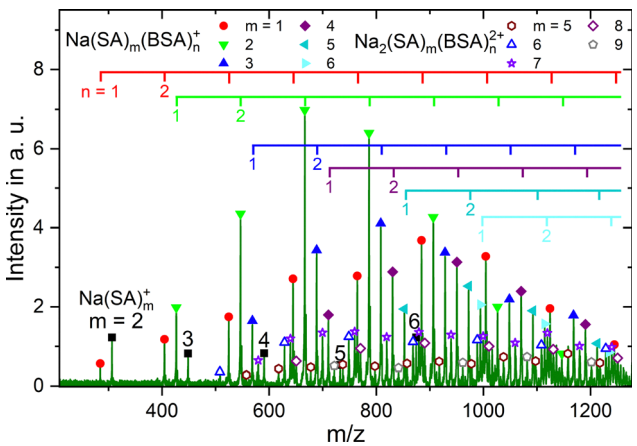

Fig. 1 Mass spectrum of mixed sulfate–bisulfate cluster ions produced by electrospray ionization of a 10 mM sodium sulfate solution in water : MeOH (1 : 1, v/v) containing 0.005% sulfuric acid. Different cluster ion compositions are observed. SA and BSA denote sulfate and bisulfate units, respectively. Pure sodium sulfate clusters are shown in black; singly and doubly charged mixed clusters are indicated by filled and open symbols, respectively.

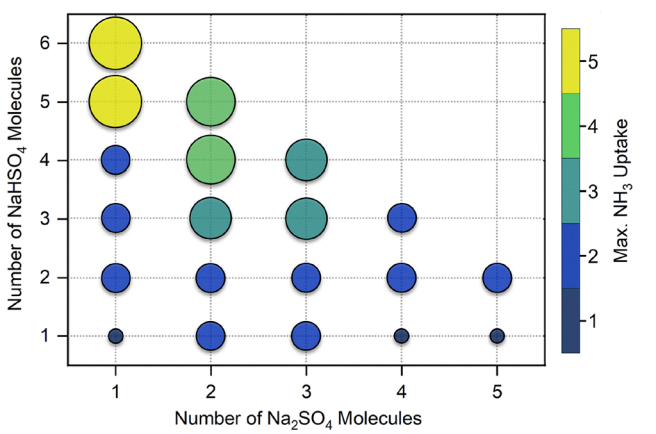

Fig. 2 Maximum number of NH_3 molecules taken up by mass selected sodium sulfate–bisulfate cluster ions as a function of their composition. The x axis shows the number of Na_2SO_4 units and the y axis the number of $NaHSO_4$ units in the cluster. The color code indicates the maximum observed ammonia uptake for each stoichiometry. White areas denote cluster compositions with signal intensities too low after mass selection for unambiguous assessment of ammonia uptake.

Open Access Article. Published on 04 June 2026. Downloaded on 6/26/2026 5:20:09 PM.
This article is licensed under a Creative Commons Attribution 3.0 Unported Licence.

number of stabilized NH_3 molecules over the investigated cluster size range. Overall, the maximum ammonia uptake correlates with the number of $NaHSO_4$ units, while the absence of one or two NH_3 uptakes in specific cluster compositions may indicate a too low ammonia adsorption energy or limited accessibility of acidic protons.

3.2 Thermochemistry of ammonia uptake

The strong correlation between ammonia uptake and bisulfate content indicates that $NaHSO_4$ plays an active role in binding NH_3 to the cluster. The acidic protons of the bisulfate moieties enable strong acid–base interactions with NH_3. Upon ammonia uptake (eqn (4)), this interaction is possibly accompanied by intracluster proton transfer, yielding an ammonium–(bi)sulfate ion pair motif (eqn (5)), *i.e.*, $[NaSO_4^-\cdots NH_4^+]$, as commonly found in ammonia–sulfuric acid cluster structures.[36,37] However, the observation of clusters containing fewer NH_3 molecules than available acidic protons suggests that the presence of an $NaHSO_4$ moiety alone is not the only factor determining ammonia uptake.

$$Na^+[Na_2SO_4]_mNaHSO_4 + NH_3 \rightarrow Na^+[Na_2SO_4]_mNaHSO_4{\cdot}NH_3 \quad (4)$$

$$Na^+[Na_2SO_4]_mNaHSO_4{\cdot}NH_3 \rightarrow Na^+[Na_2SO_4]_m[NaSO_4^-\cdots NH_4^+] \quad (5)$$

Fig. 3 shows the thermochemistry of NH_3 uptake to selected mixed sulfate/bisulfate clusters $Na^+[Na_2SO_4]_m[NaHSO_4]_n$, all calculated clusters are provided in Fig. S1 in the SI. Our calculations indicate that the Gibbs free energy of NH_3 adsorption on the studied clusters is about (−13)–(−6) kcal mol^{-1}. For smaller clusters, adsorption of NH_3 next to Na^+ is more favorable, while NH_4^+ formation is preferred for larger clusters as the NH_4^+ ions can be more efficiently incorporated into the cluster structure through Coulomb interaction with SO_4^{2-} and HSO_4^- ions. The calculations further show that uptake of a second ammonia molecule onto clusters with n = 1 is also thermodynamically favorable, however with a somewhat lower adsorption energy, see Fig. 3a and d. This indicates that HSO_4^- units are not required for ammonia adsorption to be energetically favorable, which is further supported by experimental evidence of ammonia uptake in small bare sodium sulfate clusters, $Na^+[NaSO_4]_m$ (m = 2,3), observed in the mass spectra. In other words, there seem to be sites for NH_3 available on the cluster irrespective of cluster size and composition as Na^+ ions are always available on the cluster surface, allowing NH_3 to adsorb through ion–dipole interaction. However, further studies will be needed to describe the adsorption kinetics quantitatively.

The calculated standard Gibbs free energies are summarized in Table 1, along with the values derived from the experiment based on the relative ion intensity. The agreement between experiments and theory is mostly within 3 kcal mol^{-1}, which is striking given the limitations in the evaluation of ΔG° in both approaches. The Gibbs free energy range for which the ratio of ion signals $\frac{I_{[M+NH_3^+]}}{I_{M^+}}$ lies between 0.05 and 20 is relatively narrow: at the NH_3 concentration of 1% in the buffer gas (p_{NH_3} = 0.021 Pa), it corresponds to (−10.9)–(−7.3)kcal mol^{-1};

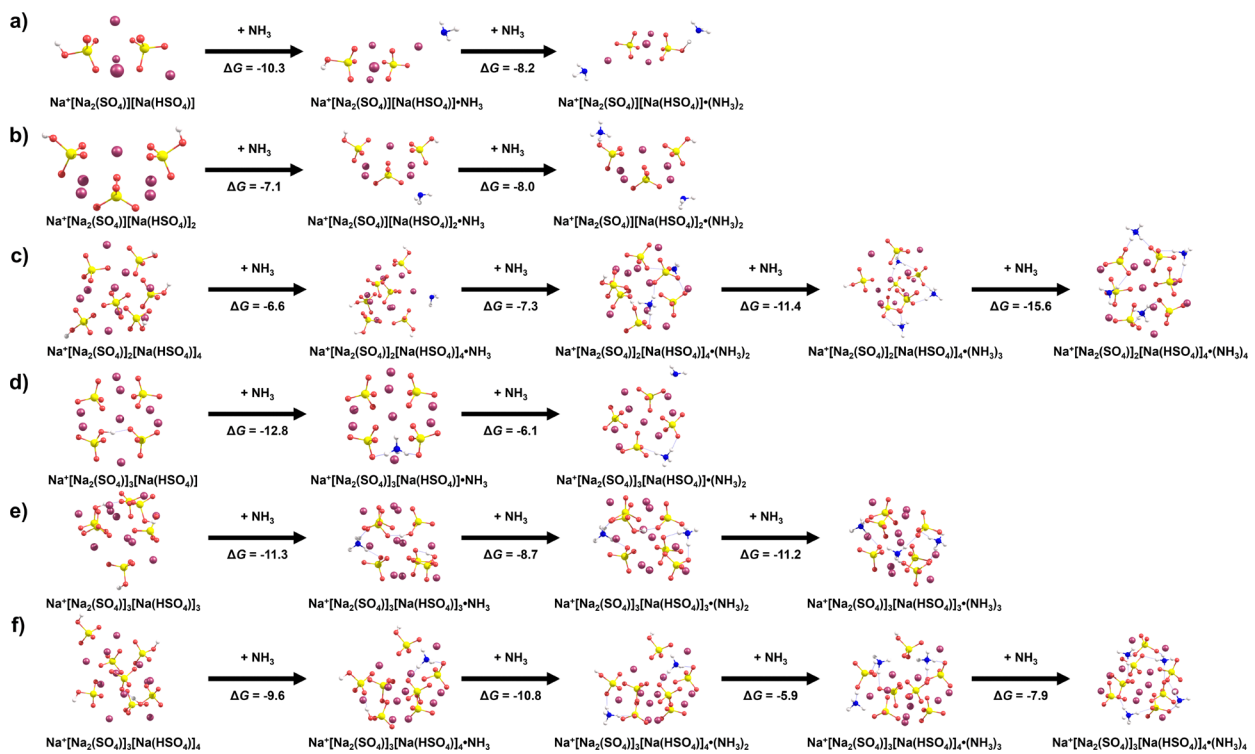

Fig. 3 Thermochemistry of ammonia (in kcal mol^{-1}) adsorption for selected $Na^+[Na_2SO_4]_m[NaHSO_4]_n$ clusters as calculated at the r^{2}SCAN-3c level. See the SI for all calculated structures.

Open Access Article. Published on 04 June 2026. Downloaded on 6/26/2026 5:20:09 PM.
This article is licensed under a Creative Commons Attribution 3.0 Unported Licence.

Table 1 Comparison of ΔG° values for NH_3 adsorption (in kcal mol^{-1}) derived from experimental data assuming that equilibrium is reached (see Table S1 for ion intensities) and from quantum chemical calculations for selected clusters. N_{NH_3} denotes the number of adsorbed NH_3 molecules, *e.g.*, N_{NH_3} = 2 corresponds to adsorption of the second NH_3 molecule on the cluster. In the experiment, NH_3 concentrations in the buffer gas of 1%, 5%, and 10% were used. For signals not observed in the experiment, the minimum ΔG° value is deduced for a signal below 3%. For the Na^+ $[Na_2SO_4]_2[NaHSO_4]_4$ cluster, the Gibbs free energy of adsorption of four NH_3 molecules is given (see also text)

Ion	N_{NH_3}	ΔG°_{exp}	ΔG°_{calc}
Na^+ $[Na_2SO_4][NaHSO_4]_2$	1	(−9.0)–(−8.0)	−7.1
	2	(−8.4)–(−7.3)	−8.0
Na^+ $[Na_2SO_4]_2[NaHSO_4]$	1	(−9.4)–(−7.5)	−9.4
	2	(−8.1)–(−7.3)	−7.1
Na^+ $[Na_2SO_4][NaHSO_4]_3$	1	(−8.8)–(−7.5)	−8.0
	2	−8.2	−7.1
	3	>−8.6	−6.8
Na^+ $[Na_2SO_4]_2[NaHSO_4]_2$	1	(−8.8)–(−7.6)	−7.5
	2	(−8.2)–(−6.7)	−10.3
Na^+ $[Na_2SO_4]_3[NaHSO_4]$	1	(−9.8)–(−8.2)	−12.8
	2	(−8.0)–(−6.8)	−6.1
Na^+ $[Na_2SO_4][NaHSO_4]_4$	1	(−8.7)–(−7.5)	−8.2
	2	(−7.4)–(−7.0)	−7.1
	3	>−7.0	−10.5
Na^+ $[Na_2SO_4]_2[NaHSO_4]_3$	1	(−8.5)–(−7.5)	−12.2
	2	(−8.0)–(−7.2)	−9.1
	3	−6.9	−9.4
Na^+ $[Na_2SO_4]_3[NaHSO_4]_2$	1	(−8.4)–(−7.6)	−9.0
	2	(−8.5)–(−6.9)	−8.5
Na^+ $[Na_2SO_4]_2[NaHSO_4]_4$	1–4	(−37.9)–(−32.9)	−40.8
Na^+ $[Na_2SO_4]_3[NaHSO_4]_3$	1	—	−11.3
	2	—	−8.7
	3	(−10.3)–(−8.7)	−11.2
Na^+ $[Na_2SO_4]_3[NaHSO_4]_4$	1	−7.5	−9.6
	2	(−9.0)–(−8.6)	−10.8
	3	(−10.1)–(−7.8)	−5.9
	4	>−6.1	−7.9

for the NH_3 concentration of 0.01%, it drops to (−13.6)–(−10.1)kcal mol^{-1}. As the energy of a single hydrogen bond is about 5 kcal mol^{-1}, the very good agreement between experiment and theory may, in part, be fortuitous.

3.3 Reaction kinetics

Kinetic measurements of ammonia uptake were carried out by monitoring the temporal evolution of reactant and product ion intensities as a function of trapping time. The rate coefficients for ammonia uptake by mass selected Na^+ $[Na_2SO_4]_m[NaHSO_4]_n$ clusters, including different compositions, are summarized in Table S2 in the SI. Under the high-pressure conditions of the ion trap, the fastest reactions, *e.g.*, those approaching the collision limit, cannot be resolved. Only the final reactant-product distribution is observed, with no detectable temporal changes in ion intensities, preventing kinetic analysis of reactions. For comparison, the collision rate coefficient for NH_3 with the Na^+ $[Na_2SO_4]_2[NaHSO_4]_3$ cluster, corresponding to the most intense peak in the spectrum, is 1.9×10^{-9} cm^3 s^{-1}, as estimated using average dipole orientation theory.[38]

The analysis first focuses on a cluster system exhibiting uptake of only one NH_3 molecule. Fig. 4 shows the normalized intensities of the parent cluster ion, *i.e.*, Na^+ $[Na_2SO_4]_3[NaHSO_4]$,

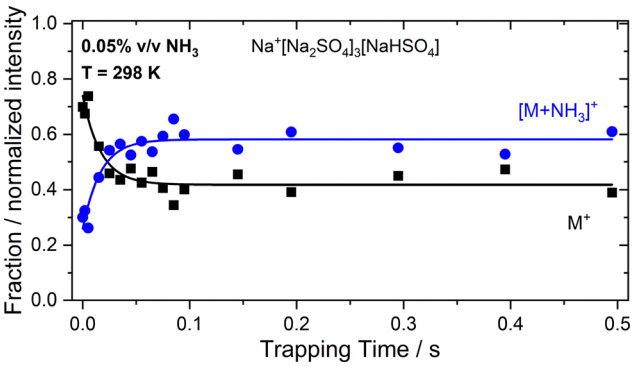

Fig. 4 Kinetics of NH_3 adsorption onto Na^+ $[Na_2SO_4]_3[NaHSO_4]$, measured at room temperature and a total pressure of 2.1 Pa (0.05% v/v NH_3 in He). The data are fitted assuming reversible NH_3 uptake.

and the corresponding ammonia adduct, $[M + NH_3]^+$, following exposure to NH_3. The decrease of the parent ion signal is accompanied by an increase of the product ion signal, consistent with reversible ammonia uptake. The data were fitted using a kinetic model that accounts for both forward (adsorption) and reverse (evaporation) processes. This analysis yields a bimolecular rate coefficient for NH_3 attachment of $k_{(1)} = 1.4 \times 10^{-10}$ cm^3 s^{-1} and a unimolecular NH_3 evaporation rate coefficient of $k_{(-1)} = 22.8$ s^{-1}, measured at a total pressure of 2.1 Pa.

The behavior observed in Fig. 4 may also be explained by the presence of cluster isomers with different reactivities. In the simplest case, one isomer reacts readily to form the ammonia adduct, whereas the other remains inert, leading to incomplete depletion of the parent ion signal and the observed kinetic plateau. The corresponding kinetic analysis yields $k_{(1)} = 2.3 \times 10^{-10}$ cm^3 s^{-1}, which is approximately 12% of the estimated collision rate. The resulting fit is essentially identical in shape to that obtained for reversible NH_3 uptake, indicating that the kinetics alone cannot differentiate between these two scenarios.

As discussed in the previous section, uptake of the polar NH_3 molecule by charged clusters is a highly efficient process driven by thermochemistry and possibly associated with the formation of the ammonium–(bi)sulfate ion pair. Our calculations shown in Fig. 3d predict that ΔG°_{calc} of NH_3 adsorption is −12.8 kcal mol^{-1}, which would correspond to the ratio of $\frac{I_{[M+NH_3]^+}}{I_{M^+}} = 23$. On the other hand, the experimental ratio of $\frac{I_{[M+NH_3]^+}}{I_{M^+}} = 0.58/0.42$ corresponds to $\Delta G^\circ_{exp} = -11.1$ kcal mol^{-1}. The agreement between the calculated and experimental free energies strongly suggests that equilibrium is indeed reached within the reaction time, without the need to invoke nonreactive isomers.

The next step is to analyze the influence of acidic protons on nucleation kinetics. Fig. 5 shows mixed sulfate–bisulfate clusters containing a total of six units with varying bisulfate-to-sulfate ratios. In line with the thermodynamic analysis, ammonia uptake is described as a sequence of reversible adsorption steps. In all three datasets, the reactant decay and final product formation are well resolved; however, intermediate species

Open Access Article. Published on 04 June 2026. Downloaded on 6/26/2026 5:20:09 PM.
This article is licensed under a Creative Commons Attribution 3.0 Unported Licence.

remain at or near the detection limit and cannot be reliably quantified. Thus, their rate coefficients are evaluated relative to the first reaction channel. Evaporation rates exhibit comparable uncertainty and sensitivity to the fitting procedure. The data can, in principle, also be described by a model that assumes the presence of isomeric species with distinct reactivities and neglects reversibility, which, particularly in cases involving multiple ammonia uptake steps, provides a more robust fit than the reversible NH_3 uptake model.

As shown in Fig. 5a, the cluster Na^+ $[Na_2SO_4]_4[NaHSO_4]_2$ undergoes sequential uptake of two NH_3 molecules. The first uptake step proceeds with a rate coefficient of 3.4×10^{-10} cm^3 s^{-1}. The primary product, *i.e.*, single NH_3 adduct, remains a minor and short-lived intermediate that is barely detected in the experiment. This behavior reflects the rapid addition of a second NH_3 molecule at near-collisional rates, combined with relatively fast unimolecular evaporation. The final product, *i.e.*, the cluster containing two ammonia molecules, seems to be more stable, exhibiting lower evaporation rates and accumulating over time toward a steady-state population.

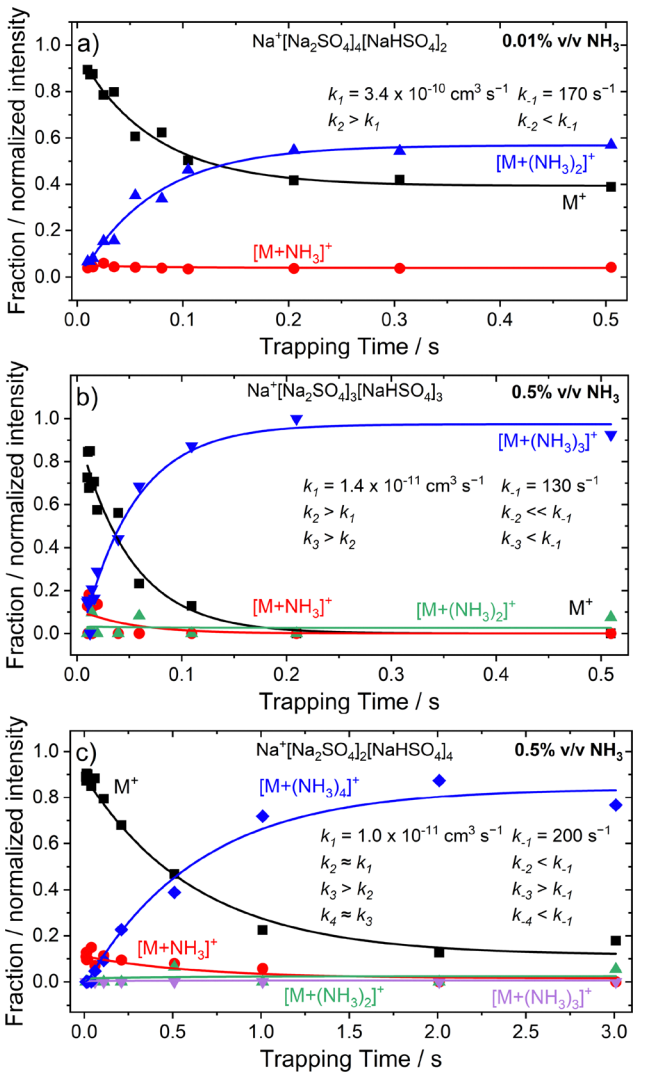

Fig. 5 Kinetic measurements of ammonia uptake by mixed sulfate–bisulfate cluster ions: (a) Na^+ $[Na_2SO_4]_4[NaHSO_4]_2$; (b) Na^+ $[Na_2SO_4]_3[NaHSO_4]_3$; and (c) Na^+ $[Na_2SO_4]_2[NaHSO_4]_4$. The data are fitted assuming reversible NH_3 uptake.

For Na^+ $[Na_2SO_4]_3[NaHSO_4]_3$, where one additional acidic proton is present, three consecutive ammonia uptake steps occur. The first uptake proceeds with a rate coefficient of 1.4×10^{-11} cm^3 s^{-1}, followed by faster second and third uptake steps. Evaporation rates decrease upon ammonia uptake, indicating enhanced cluster stabilization. Finally, the cluster Na^+ $[Na_2SO_4]_2[NaHSO_4]_4$ undergoes four consecutive NH_3 uptake steps. The first step proceeds with a rate coefficient of 1.0×10^{-11} cm^3 s^{-1}, followed by a second step with a comparable rate. The third and fourth steps are significantly faster. The evaporation rates are consistent with the previous case, indicating that ammonia addition stabilizes the cluster against evaporation. The only exception is k_{-3}, which is slightly higher than k_{-1}; however, this likely reflects uncertainties associated with low-intensity signals close to the signal-to-noise limit. Quantum chemical calculations predict here the ratio of $[M]^+ : [M + NH_3]^+ : [M + (NH_3)_2]^+ : [M + (NH_3)_3]^+ : [M + (NH_3)_4]^+ = 1 : 0.008 : 0.0001 : 0.004 : 96$, with the overall reaction Gibbs free energy for adsorption of four NH_3 molecules of $\Delta G^\circ_{calc} = -40.8$ kcal mol^{-1} (Fig. 3c). The experimental Gibbs free energy is evaluated from the ratio of $[M]^+ : [M + (NH_3)_4]^+ = 15 : 85$ as $\Delta G^\circ_{exp} = -39.1$ kcal mol^{-1}, at higher pressures we get (−37.9)–(−32.9) kcal mol^{-1}, see Table 1.

Comparison of the three cluster ions, differing only in the number of acidic protons, reveals three key kinetic features. First, cluster composition strongly influences the overall uptake rate. While Na^+ $[Na_2SO_4]_3[NaHSO_4]_3$ and Na^+ $[Na_2SO_4]_2[NaHSO_4]_4$ exhibit comparable rate coefficients for the first uptake step, Na^+ $[Na_2SO_4]_4[NaHSO_4]_2$ is approximately an order of magnitude faster, despite its similar cluster size. Second, in all three systems, the first NH_3 uptake is rate-limiting, followed by faster subsequent steps. Third, the addition of the first NH_3 molecule to the sulfate–bisulfate cluster typically leads to suppressed evaporation rates during subsequent ammonia uptake steps.

These observations demonstrate that ion trap experiments under multicollisional conditions provide a suitable model system for nucleation studies, in which even small changes in cluster composition can be directly correlated with changes in nucleation kinetics. This provides valuable experimental data for comparison with computational studies of ion-induced nucleation. However, the measured rate coefficients cannot be directly extrapolated to atmospheric conditions, as effects such as third-body stabilization and cluster hydration are not explicitly accounted for under the present experimental conditions.

3.4 Influence of NH_3 partial pressure on reactant–adduct distribution

Ion trap experiments performed under multicollisional conditions provide a set of complementary measurements to test the proposed reaction mechanisms. Our previous studies have shown that temperature-dependent measurements and kinetic isotope effects can help assign the observed kinetic behavior to

This journal is © the Owner Societies 2026

Open Access Article. Published on 04 June 2026. Downloaded on 6/26/2026 5:20:09 PM.
This article is licensed under a Creative Commons Attribution 3.0 Unported Licence.

the correct mechanism.[39] In the present study, the agreement between experimental and computational Gibbs free energies indicates that NH_3 uptake onto mixed sulfate–bisulfate clusters is thermodynamically favorable. This can occur either through simple NH_3 adsorption or *via* formation of an ammonium–(bi)sulfate ion pair under equilibrium conditions. At the same time, the kinetic data can be interpreted using a model that assumes the presence of cluster isomers with different reactivities, as discussed in the previous section. To test this interpretation, we performed experiments in which the NH_3 partial pressure in a helium carrier gas was varied while the total pressure was kept constant at 2.1 Pa. If two isomers are present, namely one reactive and one inert, and the reaction proceeds irreversibly, the NH_3 partial pressure should affect the reaction rates but not the final plateau values in the kinetic traces, *i.e.*, the steady-state distribution of reactants and adducts. In contrast, if NH_3 uptake is reversible, increasing the NH_3 concentration should shift the equilibrium toward higher abundances of ammonia adducts.

Fig. 6 shows the ammonia uptake kinetics for Na^+ $[Na_2SO_4]_3$-$[NaHSO_4]_4$, which can accommodate up to three ammonia molecules. The kinetic traces follow a typical pattern, with the first ammonia uptake step being the slowest, while subsequent additions proceed significantly faster. At an ammonia concentration of 0.05% (v/v) in helium, the reaction gradually reaches a plateau after approximately 0.3 s. At this point, the intensity ratio between the mixed sulfate–bisulfate cluster and the ammonia adduct is approximately 2 : 3 in favor of the doped cluster, and this ratio remains constant thereafter. Increasing the ammonia concentration to 0.5% leads to a significant shift in the distribution, with ammonia adducts becoming dominant. This behavior reveals a change in product distribution relative to the lower ammonia concentration and suggests that the system approaches an equilibrium-like steady state, where higher NH_3 levels favor ammonia adduct formation. The similar rate coefficients obtained at both concentrations indicate that the intrinsic reaction kinetics remain largely unchanged. Instead, the final reactant-product distribution is governed by the NH_3 concentration. A similar behavior is observed for other clusters, *e.g.*, Na^+ $[Na_2SO_4]_3[NaHSO_4]_3$ (Fig. S3), which further supports the conclusion, derived from Gibbs free energy calculations, that ammonia uptake occurs under equilibrium conditions.

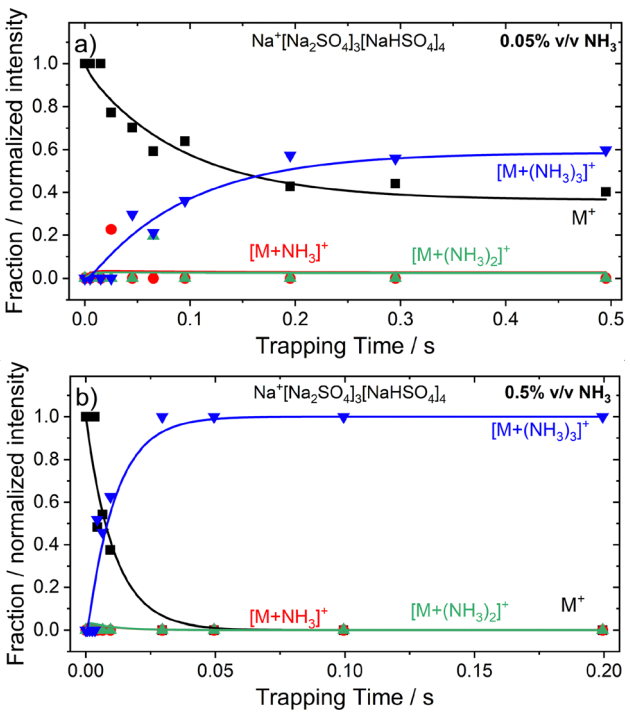

Fig. 6 Kinetics of NH_3 uptake by Na^+ $[Na_2SO_4]_3[NaHSO_4]_4$ cluster ions (m/z = 928.6) exposed to NH_3/He gas mixtures containing (a) 0.05% and (b) 0.5% (v/v) ammonia.

However, increasing the pressure does not always lead to such a pronounced effect. For example, in the kinetic measurements of Na^+ $[Na_2SO_4]_2[NaHSO_4]_4$ (Fig. S4), despite doubling the ammonia concentration, the final reactant-product ratio remains approximately 1 : 4 in favor of the ammonia adduct. The independence of this ratio from ammonia concentration in this case supports the proposed mechanism involving two cluster isomers with distinct reactivities, although it may also be explained by a slow establishment of equilibrium.

To further assess this behavior, the plateau formation was analyzed for each cluster size. This enables direct evaluation of the final reactant–product partitioning under varying ammonia partial pressures. The resulting distributions of reactant clusters and their corresponding ammonia adducts are summarized in Table S1 in the SI. These data were also used to derive the experimental Gibbs free energies reported in Table 1. The measurements were conducted at NH_3 concentrations of 0.1%, 1%, 5%, and 10%, while the total pressure was kept at 2.1 Pa. The mass spectra of the cluster composition were recorded at a trapping time of 400 ms up to 3 s, at which the cluster distributions have reached their final composition.

Most reactant-to-product ratios depend on ammonia concentration, particularly between 0.1% and 1.0%, which in many cases leads to substantial changes. Only a few mass-selected clusters seem to be independent of concentration. In particular, Na^+ $[Na_2SO_4]_2[NaHSO_4]$ and Na^+ $[Na_2SO_4]_4[NaHSO_4]_2$ show nearly constant ratios across the full concentration range. The strongest concentration effects are observed for bisulfate-rich clusters, such as Na^+ $[Na_2SO_4][NaHSO_4]_{5,6}$. These clusters are predominantly ammonia-free at low concentrations but increasingly form ammonia adducts as the concentration rises. Nevertheless, for most clusters, the changes are moderate, and higher ammonia concentrations lead to a gradual increase in adduct formation. This behavior supports reversible ammonia uptake, as an assumption of reactive and non-reactive cluster isomers cannot explain the pressure dependent change in adduct formation.

An interesting pattern is observed across the cluster series. Smaller clusters ($m/z < 700$) retain substantial fractions ($\geq$50%) of ammonia-free species across all concentrations and typically bind only a single ammonia molecule. Intermediate-sized clusters, such as Na^+ $[Na_2SO_4][NaHSO_4]_5$ and Na^+ $[Na_2SO_4]_2[NaHSO_4]_4$, undergo a transition from ammonia-free or singly doped species at low concentrations to near-saturation at higher concentrations. In

Open Access Article. Published on 04 June 2026. Downloaded on 6/26/2026 5:20:09 PM. This article is licensed under a Creative Commons Attribution 3.0 Unported Licence.

contrast, larger clusters ($m/z > 800$) are nearly fully covered by ammonia even at the lowest concentrations. This systematic trend indicates a size-dependent change in the ammonia binding motif, in agreement with computational results, from direct NH_3 adsorption near Na^+ in smaller clusters to the preferential formation of ammonium–(bi)sulfate ion pairs in larger clusters.

4 Conclusions

Ammonia uptake by mixed sodium sulfate–bisulfate cluster cations was investigated using ion trap mass spectrometry under multicollisional conditions. Mass selection of individual cluster compositions enabled a direct assessment of how sulfate and bisulfate units influence ammonia uptake behavior. The maximum ammonia uptake correlates with the number of bisulfate units, whereas the reaction kinetics show a stronger dependence on the sulfate content.

Quantum chemical calculations indicate that ammonia uptake by sodium sulfate–bisulfate cluster ions is primarily governed by thermodynamics. Bisulfate units enhance uptake through acid–base interactions and facilitate proton transfer to form ammonium–(bi)sulfate ion pairs. However, such proton transfer is not a prerequisite for energetically favorable adsorption. The agreement between experimental and calculated Gibbs free energies indicates that the system approaches equilibrium under the experimental conditions and thus supports a reversible NH_3 uptake mechanism. This is further supported by the clear dependence of steady-state cluster ratios on NH_3 concentration for most mass-selected clusters, with increasing ammonia adduct signals at higher partial pressures. Kinetic measurements reveal sequential uptake, with the first adsorption step being rate-limiting. The initial NH_3 uptake typically stabilizes the clusters by reducing evaporation in subsequent steps. Overall, these results point to the importance of cluster composition in controlling early-stage particle formation.

The present work demonstrates a significant advancement in the application of the ion trap techniques to nucleation studies. By operating under multicollisional conditions, the experiments probe cluster growth close to equilibrium, in contrast to conventional ion trap studies performed under (ultra)high-vacuum conditions, thereby enabling access to both uptake kinetics and evaporation-related processes for mass-selected charged particles. Despite the simplified treatment of atmospheric-pressure effects, particularly the absence of third-body stabilization in the measured kinetics, this experimental approach provides a valuable complement to aerosol chamber and flow tube experiments. It, therefore, opens new avenues for future investigations of the molecular-level mechanisms governing ion-induced atmospheric particle formation in chemically complex systems involving sulfuric acid, ammonia, amines, and oxidized organic molecules.

Author contributions

K. L. (experiment): investigation, formal analysis, writing; G. S. (theory): methodology, formal analysis, writing; M. O. (theory): conceptualization, investigation, methodology, formal analysis, writing; J. L. (experiment): methodology, conceptualization, supervision, resources, writing.

Conflicts of interest

There are no conflicts to declare.

Data availability

All data supporting the findings of this study are available in the supplementary information (SI), including Cartesian coordinates and Gibbs free energies of all calculated structures. Supplementary information is available. See DOI: https://doi.org/10.1039/d6cp01436d.

Further details will be provided by the corresponding author upon a reasonable request.

Acknowledgements

This work was funded by the German Research Foundation (Deutsche Forschungsgemeinschaft, DFG) through the Emmy Noether Programme (Project No. 442679477). The computational results presented have been obtained using the HPC infrastructure LEO of the University of Innsbruck. GS acknowledges receipt of a DOC Fellowship of the Austrian Academy of Sciences.

References

1 O. Boucher, D. Randall, P. Artaxo, C. Bretherton, G. Feingold, P. Forster, V.-M. Kerminen, Y. Kondo, H. Liao, U. Lohmann, P. Rasch, S. K. Satheesh, S. Sherwood, B. Stevens and X. Y. Zhang, *Climate Change 2013: The Physical Science Basis. Contribution of Working Group I to the Fifth Assessment Report of the Intergovernmental Panel on Climate Change*, Cambridge University Press, Cambridge, United Kingdom, 2013, pp. 571–658.

2 *Climate Change 2021: The Physical Science Basis. Contribution of Working Group I to the Sixth Assessment Report of the Intergovernmental Panel on Climate Change*, ed. V. Masson-Delmotte, P. Zhai, A. Pirani, S. L. Connors, C. Péan, S. Berger, N. Caud, Y. Chen, L. Goldfarb, M. I. Gomis, M. Huang, K. Leitzell, E. Lonnoy, J. B. R. Matthews, T. K. Maycock, T. Waterfield, O. Yelekçi, R. Yu and B. Zhou, Cambridge University Press, Cambridge, United Kingdom, 2021.

3 R. Zhang, A. Khalizov, L. Wang, M. Hu and W. Xu, *Chem. Rev.*, 2012, **112**, 1957–2011.

4 M. Kulmala, J. Kontkanen, H. Junninen, K. Lehtipalo, H. E. Manninen, T. Nieminen, T. Petäjä, M. Sipilä, S. Schobesberger, P. Rantala, A. Franchin, T. Jokinen, E. Järvinen, M. Aijälä, J. Kangasluoma, J. Hakala, P. P. Aalto, P. Paasonen, J. Mikkilä, J. Vanhanen, J. Aalto, H. Hakola, U. Makkonen, T. Ruuskanen, R. L. Mauldin III, J. Duplissy, H. Vehkamäki, J. Bäck, A. Kortelainen, I. Riipinen, T. Kurten, M. V. Johnston, J. N. Smith, M. Ehn, T. F. Mentel, K. E. J. Lehtinen, A. Laaksonen, V.-M. Kerminen and D. R. Worsnop, *Science*, 2013, **339**, 943–946.

Open Access Article. Published on 04 June 2026. Downloaded on 6/26/2026 5:20:09 PM. This article is licensed under a Creative Commons Attribution 3.0 Unported Licence.

5 S. M. Ball, D. R. Hanson, F. L. Eisele and P. H. McMurry, *J. Geophys. Res.: Atmos.*, 1999, **104**, 23709–23718.
6 D. R. Benson, M. E. Erupe and S.-H. Lee, *Geophys. Res. Lett.*, 2009, **36**, L15818.
7 J. Kirkby, J. Curtius, J. Almeida, E. Dunne, J. Duplissy, S. Ehrhart, A. Franchin, S. Gagne, L. Ickes, A. Kürten, A. Kupc, A. Metzger, F. Riccobono, L. Rondo, S. Schobesberger, G. Tsagkogeorgas, D. Wimmer, A. Amorim, F. Bianchi, M. Breitenlechner, A. David, J. Dommen, A. Downard, M. Ehn, R. C. Flagan, S. Haider, A. Hansel, D. Hauser, W. Jud, H. Junninen, F. Kreissl, A. Kvashin, A. Laaksonen, K. Lehtipalo, J. Lima, E. R. Lovejoy, V. Makhmutov, S. Mathot, J. Mikkilä, P. Minginette, S. Mogo, T. Nieminen, A. Onnela, P. Pereira, T. Petäjä, R. Schnitzhofer, J. H. Seinfeld, M. Sipilä, Y. Stozhkov, F. Stratmann, A. Tome, J. Vanhanen, Y. Viisanen, A. Vrtala, P. E. Wagner, H. Walther, E. Weingartner, H. Wex, P. M. Winkler, K. S. Carslaw, D. R. Worsnop, U. Baltensperger and M. Kulmala, *Nature*, 2011, **476**, 429–433.
8 W. A. Glasoe, K. Volz, B. Panta, N. Freshour, R. Bachman, D. R. Hanson, P. H. McMurry and C. Jen, *J. Geophys. Res.: Atmos.*, 2015, **120**, 1933–1950.
9 A. Kürten, S. Münch, L. Rondo, F. Bianchi, J. Duplissy, T. Jokinen, H. Junninen, N. Sarnela, S. Schobesberger, M. Simon, M. Sipilä, A. Amorim, J. Dommen, N. M. Donahue, E. M. Dunne and O. Signs, *Atmos. Chem. Phys.*, 2015, **15**, 10701–10721.
10 K. Lehtipalo, C. Yan, L. Dada, F. Bianchi, M. Xiao, R. Wagner, D. Stolzenburg, L. R. Ahonen, A. Amorim, A. Baccarini, P. S. Bauer, B. Baumgartner, A. Bergen, A.-K. Bernhammer, M. Breitenlechner, S. Brilke, A. Buchholz, S. Buenrostro Mázon, D. Chen, X. Chen, A. Dias, J. Dommen, D. C. Draper, J. Duplissy, M. Ehn, H. Finkenzeller, L. Fischer, C. Frege, C. Fuchs, O. Garmash, H. Gordon, J. Hakala, X. He, L. Heikkinen, M. Heinritzi, J. C. Helm, V. Hofbauer, C. R. Hoyle, T. Jokinen, J. Kangasluoma, V.-M. Kerminen, C. Kim, J. Kirkby, J. Kontkanen, A. Kürten, M. J. Lawler, H. Mai, S. Mathot, R. L. Mauldin, U. Molteni, L. Nichman, W. Nie, T. Nieminen, A. Ojdanic, A. Onnela, M. Passananti, T. Petäjä, F. Piel, V. Pospilov, L. L. J. Quelever, M. P. Rissanen, C. Rose, N. Sarnela, S. Schallhart, S. Schuchmann, K. Sengupta, M. Simon, M. Sipilä, C. Tauber, A. Tome, J. Tröstl, O. Väisänen, A. L. Vogel, R. Volkamer, A. C. Wagner, M. Wang, L. Weitz, D. Wimmer, P. Ye, A. Ylisirniö, Q. Zha, K. S. Carslaw, J. Curtius, N. M. Donahue, R. C. Flagan, A. Hansel, I. Riipinen, A. Virtanen, P. M. Winkler, U. Baltensperger, M. Kulmala and D. R. Worsnop, *Sci. Adv.*, 2018, **4**, eaau5363.
11 M. Wang, W. Kong, R. Marten, X.-C. He, D. Chen, J. Pfeifer, A. Heitto, J. Kontkanen, L. Dada, A. Kürten, T. Yli-Juuti, H. E. Manninen, S. Amanatidis, A. Amorim, R. Baalbaki, A. Baccarini, D. M. Bell, B. Bertozzi, S. Bräkling, S. Brilke, L. C. Murillo, R. Chiu, B. Chu, L.-P. D. Menezes, J. Duplissy, H. Finkenzeller, L. G. Carracedo, M. Granzin, R. Guida, A. Hansel, V. Hofbauer, J. Krechmer, K. Lehtipalo, H. Lamkaddam, M. Lampimäki, C. P. Lee, V. Makhmutov, G. Marie, S. Mathot, R. L. Mauldin, B. Mentler, T. Müller, A. Onnela, E. Partoll, T. Petäjä, M. Philippov, V. Pospisilova, A. Ranjithkumar, M. Rissanen, B. Rörup, W. Scholz, J. Shen, M. Simon, M. Sipilä, G. Steiner, D. Stolzenburg, Y. J. Tham, A. Tome, A. C. Wagner, D. S. Wang, Y. Wang, S. K. Weber, P. M. Winkler, P. J. Wlasits, Y. Wu, M. Xiao, Q. Ye, M. Zauner-Wieczorek, X. Zhou, R. Volkamer, I. Riipinen, J. Dommen, J. Curtius, U. Baltensperger, M. Kulmala, D. R. Worsnop, J. Kirkby, J. H. Seinfeld, I. El-Haddad, R. C. Flagan and N. M. Donahue, *Nature*, 2020, **581**, 184–189.
12 M. Wang, M. Xiao, B. Bertozzi, G. Marie, B. Rörup, B. Schulze, R. Bardakov, X.-C. He, J. Shen, W. Scholz, R. Marten, L. Dada, R. Baalbaki, B. Lopez, H. Lamkaddam, H. E. Manninen, A. Amorim, F. Ataei, P. Bogert, Z. Brasseur, L. Caudillo, L.-P. D. Menezes, J. Duplissy, A. M. L. Ekman, H. Finkenzeller, L. G. Carracedo, M. Granzin, M. H. R. Guida, V. Hofbauer, K. Höhler, K. Korhonen, J. E. Krechmer, A. Kürten, K. Lehtipalo, N. G. A. Mahfouz, V. Makhmutov, D. Massab, S. Mathot, R. L. Mauldin, T. M. B. Mentler, A. Onnela, T. Petäjä, M. Philippov, A. A. Piedehierro, A. Pozzer, A. Ranjithkumar, M. Schervish, S. Schobesberger, M. Simon, Y. Stozhkov, A. Tome, N. S. Umo, F. Vogel, R. Wagner, D. S. Wang, S. K. Weber, A. Welti, Y. Wu, M. Zauner-Wieczorek, M. Sipilä, P. M. Winkler, A. Hansel, U. Baltensperger, M. Kulmala, R. C. Flagan, J. Curtius, I. Riipinen, H. Gordon, J. Lelieveld, I. El-Haddad, R. Volkamer, D. R. Worsnop, T. Christoudias, J. Kirkby, O. Möhler and N. M. Donahue, *Nature*, 2022, **605**, 483–489.
13 T. Kurten, V. Loukonen, H. Vehkamäki and M. Kulmala, *Atmos. Chem. Phys.*, 2008, **8**, 4095–4103.
14 C. N. Jen, P. H. McMurry and D. R. Hanson, *J. Geophys. Res.: Atmos.*, 2014, **119**, 7502–7514.
15 T. Olenius, R. Halonen, T. Kurten, H. Henschel, O. Kupiainen-Määttä, I. K. Ortega, C. N. Jen, H. Vehkamäki and I. Riipinen, *J. Geophys. Res.: Atmos.*, 2017, **122**, 7103–7118.
16 H. Yu, R. McGraw and S.-H. Lee, *Geophys. Res. Lett.*, 2012, **39**, L02807.
17 S. E. Harold, C. J. Bready, L. A. Juechter, L. A. Kurfman, S. Vanovac, V. R. Fowler, G. E. Mazaleski, T. T. Odbadrakh and G. C. Shields, *J. Phys. Chem. A*, 2022, **126**, 1718–1728.
18 N. Myllys, S. Chee, T. Olenius, M. Lawler and J. Smith, *J. Phys. Chem. A*, 2019, **123**, 2420–2425.
19 L. M. McInnes, D. S. Covert, P. K. Quinn and M. S. Germani, *J. Geophys. Res.: Atmos.*, 1994, **99**, 8257–8268.
20 D. O. De Haan, T. Brauers, K. W. Oum, J. Stutz, T. Nordmeyer and B. J. Finlayson-Pitts, *Int. Rev. Phys. Chem.*, 1999, **18**, 343–385.
21 B. Alexander, R. J. Park, D. J. Jacob, Q. B. Li, R. M. Yantosca, J. Savarino, C. C. W. Lee and M. H. Thiemens, *J. Geophys. Res.: Atmos.*, 2005, **110**, D10307.
22 J. W. Chi, W. J. Li, D. Z. Zhang, J. C. Zhang, Y. T. Lin, X. J. Shen, J. Y. Sun, J. M. Chen, X. Y. Zhang, Y. M. Zhang and W. X. Wang, *Atmos. Chem. Phys.*, 2015, **15**, 11341–11353.
23 M. E. Cooke, A. R. Alotbi, C. M. Waters, L. J. Heagle, N. C. Armstrong, C. J. Poworoznek, Z. Zhang, A. Gold, J. D. Surratt and A. P. Ault, *J. Phys. Chem. A*, 2025, **129**, 7451–7460.
24 M. E. Cooke, N. C. Armstrong, Z. Lei, Y. Chen, C. M. Waters, Y. Zhang, N. A. Buchenau, M. Q. Dibley, I. R. Ledsky, T. Szalkowski, J. Y. Lee, K. Baumann, Z. Zhang, W. Vizuete, A. Gold, J. D. Surratt and A. P. Ault, *ACS Earth Space Chem.*, 2022, **6**, 2790–2800.

Open Access Article. Published on 04 June 2026. Downloaded on 6/26/2026 5:20:09 PM.
This article is licensed under a Creative Commons Attribution 3.0 Unported Licence.

25 B. R. Bzdek, D. P. Ridge and M. V. Johnston, *J. Phys. Chem. A*, 2010, **114**, 11638–11644.
26 B. R. Bzdek, D. P. Ridge and M. V. Johnston, *Atmos. Chem. Phys.*, 2010, **10**, 3495–3503.
27 B. R. Bzdek, J. W. DePalma and M. V. Johnston, *Acc. Chem. Res.*, 2017, **50**, 1965–1975.
28 J. C. Hartmann, J. Y. Lim, Y. Sheng, M. Reimann, S. J. Madlener, C. van der Linde, C.-K. Siu and M. K. Beyer, *Angew. Chem., Int. Ed.*, 2026, **65**, e20403.
29 K. Li, Y. Yan and J. Lengyel, *Aerosol Sci. Technol*, 2026, DOI: 10.1080/02786826.2026.2633182.
30 Y. Yan, L. Schmitt, A. Khramchenkova and J. Lengyel, *J. Mass Spectrom.*, 2023, **58**, e4955.
31 G. Schöpfer, M. Gatt and M. Oncák, *Genetic algorithms*, https://git.uibk.ac.at/c7441332/genetic-algorithms, 2026.
32 C. Bannwarth, E. Caldeweyher, S. Ehlert, A. Hansen, P. Pracht, J. Seibert, S. Spicher and S. Grimme, *WIREs Comput. Mol. Sci.*, 2020, **11**, e01493.
33 C. Bannwarth, S. Ehlert and S. Grimme, *J. Chem. Theory Comput.*, 2019, **15**, 1652–1671.
34 S. Grimme, A. Hansen, S. Ehlert and J. Mewes, *J. Chem. Phys.*, 2020, **154**, 064103.
35 F. Neese, *WIREs Comput. Mol. Sci.*, 2025, **15**, e70019.
36 K. D. Froyd and E. R. Lovejoy, *J. Phys. Chem. A*, 2012, **116**, 5886–5899.
37 C. J. Johnson and M. A. Johnson, *J. Phys. Chem. A*, 2013, **117**, 13265–13274.
38 T. Su and M. T. Bowers, *J. Chem. Phys.*, 1973, **58**, 3027–3037.
39 N. Levin, J. Lengyel, J. F. Eckhard, M. Tschurl and U. Heiz, *J. Am. Chem. Soc.*, 2020, **142**, 5862–5869.

 This journal is © the Owner Societies 2026